Pulses of Cold Atlantic Water in the Arctic Ocean from Ocean Model Simulation

Chuanshuai Fu[1], Clark Pennelly[1], Yarisbel Garcia-Quintana[1] and Paul G. Myers[1]

[1] Department of Earth and Atmospheric Sciences, University of Alberta, Edmonton, Alberta, Canada

Corresponding author: Chuanshuai Fu (mailto:chuanshu@ualberta.ca)

Key Points:

- A cold mode of Atlantic Water (CAW) with temperature below 0 ℃ that greatly reduced the heat content of the eastern Arctic, is identified
- The source of the CAW is primarily from the Barents Sea Branch Water, with secondary contributions from the Fram Strait Branch Water
- Sea surface cooling during 2013-2014 within the Barents Sea provided critical preconditioning for the transformation into CAW

Abstract

The thermohaline intrusion of the warm and saline Atlantic Water (AW) into the Arctic Ocean, referred to as "Arctic Atlantification", has significant implications and feedback to the dynamics and thermodynamics of the Arctic Ocean. The AW enters the Arctic Ocean through two gateways: Fram Strait and the Barents Sea Opening (BSO). The relative strength of these two AW branches dominates the oceanic heat contribution to the Arctic Ocean. In conjunction with the measurements in key hydrographic sections, numerical ocean modelling provides us with a useful tool to characterize and corroborate the temporal and spatial variability of the AW branches. Simulations are conducted using the regional configuration Arctic and North Hemispheric Atlantic (ANHA) of the ocean/sea-ice model NEMO running at 1/4° and 1/12° resolution. Online passive tracers from the model configuration are used to trace the pathways of the AW inflow in the Arctic Ocean. With the AW becoming more important to the dynamics of the Arctic Ocean, this study aims to examine its variability, transformation, impacts, and ultimately track how it evolves. While the heat in the Fram Strait Branch Water (FSBW) dissipates in a slower process through the mixing with the ambient cold water below sea surface, the vast majority of the heat loss of the Barents Sea Branch Water (BSBW) takes place in Barents Sea due to the sea surface cooling, leading to Cold Atlantic Water (CAW) production during 2013 and 2014. The CAW pulses result in a significant heat content reduction in the eastern Arctic.

Plain Language Summary

Atlantic Water (AW) is a warm and salty water mass that distinguishes itself from the cold and fresh Arctic Water. The AW flows into the Arctic Ocean in two branches, Fram Strait Branch Water (FSBW) and Barents Sea Branch

Water (BSBW). Numerical modelling is an effective tool to simulate the AW based on its thermohaline properties. We first evaluate the interannual and seasonal variability of the AW thermohaline structure at these two gateways, then quantify the AW volume and heat transport on the interannual and seasonal timescales. We also compare long-term transport means with the available observations. We discover two strong Cold Atlantic Water (CAW) anomaly events along the rim of the eastern Eurasian Basin in 2013 and 2014, overturning our understanding that the AW is always warm and saline. The dominant contributor to the CAW formation is the intense sea surface cooling in the Barents Sea for two consecutive years. Releasing artificial particles at Fram Strait and the BSO, we find that the source of the CAW is primarily from the BSBW. The CAW signals progress along the typical AW poleward pathway and eventually reduce the heat that is contained in the AW layer of the eastern Arctic Basin.

1 Introduction

The Arctic Ocean resembles an isolated Mediterranean Sea - two deep basins, divided by the Lomonosov Ridge, sit at the centre: the Canadian and Eurasian Basins with average depths of roughly 4000 m (Figure 1). Shallow continental shelves are found on the periphery defining the Arctic marginal seas (Figure 1). Other than receiving the freshwater from river runoff from the surrounding landmasses and more precipitation than evaporation, it also receives Pacific-origin inflow (Pacific Water, hereafter PW) via Bering Strait and Atlantic-origin inflow (Atlantic Water, hereafter AW) through Fram Strait and the Barents Sea Opening (BSO). AW is a typically warm and saline water mass that originates from the Northern Atlantic Ocean. Therefore, these two AW branches, carrying the Fram Strait Branch Water (FSBW) and the Barents Sea Branch Water (BSBW), transport a great amount of heat and salt into the cold and relatively fresh Arctic Ocean. The AW forms an intermediate layer (~200-1000 m) in the Arctic basins with a maximum temperature of up to about 1℃, fed by the warm and salty FSBW and the relatively cool and less saline BSBW. The BSBW mixes with and partially subducts below the warm core of the FSBW (Pérez-Hernández et al., 2019; Li et al., 2020). For the upper layer, the surface mixed layer is thin, with a normal thickness of 5-10 m throughout the Arctic Ocean (Woodgate, 2013). Unlike the Canadian Basin that has a stronger stratification, in the Eurasian Basin, there is no PW band but a thicker cold Atlantic halocline. The halocline separates the AW layer from the surface mixed layer and limits the vertical heat flux from the warmer AW layer to the surface mixed layer. Below the AW layer is the cold and saline Arctic Bottom Water (Woodgate, 2013). The water density of the Arctic Ocean is mainly determined by the salinity based on the non-linear equation of state, so salinity changes have a more profound impact on modifying the stratification than ocean temperature changes (Carmack, 2007). However, the thermodynamic impact is amplifying as the Arctic has been warming under the effect of global warming and Arctic amplification. According to model studies and observations, the oceanic heat transport to the Arctic Ocean via AW through Fram Strait and the BSO has increased during recent decades (Beszczynska-Möller, 2012; Muilwijk et al., 2018; Spielhagen et

al., 2011; Wang et al., 2019, 2020). The Arctic Ocean has demonstrated a rapid downward trend of minimum sea ice cover at the end of the summer for the last several decades (Cavalieri & Parkinson, 2012; Comiso, 2012; Comiso et al., 2017; Stroeve et al., 2007), and has shown an ongoing acceleration in the decline of the Arctic sea ice cover (Cavalieri & Parkinson, 2012; Stroeve et al., 2007). They also diagnose a thinning of the average Arctic multiyear ice cover (Comiso, 2012; Spreen et al., 2020). All these signs indicate a warming world and the possibility of an ice-free Arctic Ocean (less than 10^6 km^2) in summer as early as 2030-2050 (Guarino et al., 2020).

Fram Strait is one of the Arctic gateways, between Greenland and Svalbard. It is one of two important sections for evaluating the variability of the AW entering the Arctic Ocean (Beszczynska-Moller, 2012). The warm and salty AW that flows into the Arctic Ocean is carried by the northward flowing West Spitsbergen Current (WSC) through Fram Strait. Some portion of the AW recirculates back to the south through several recirculation pathways south of $81^{\circ}N$ and mostly subducts underneath the Arctic Water (ArW) advected by the southward flowing East Greenland Current (EGC). This is primarily achieved by the spawning of the abundant mesoscale eddies (with the Rossby radius of deformation of 3-6 km) near Fram Strait (Wekerle et al., 2020). The AW flowing into the Arctic Basin through Fram Strait splits into three major pathways: the shallow Svalbard Branch along the Svalbard continental slope at 400-500 m depth (~0.8 Sv), the Yermak Pass Branch that flows across the Yermak Plateau at 700-800 m depth (~1.9 Sv), and a relatively minor component comprising the deep Yermak Branch following the western slope of the Yermak Plateau along ~1000 m isobath (~0.1 Sv) (Crews et al., 2019; Menze et al., 2019; Pérez-Hernández et al., 2019). These three branches vary on the seasonal and interannual time scales. Ultimately, they merge east of the Yermak Plateau and form the FSBW that flows along the rim of the Eurasian Basin (Athanase et al., 2020). The AW is cooled and freshened near Fram Strait through a suite of processes such as the sea ice melt, winter convection, lateral eddy fluxes as well as exchanges with shelf waters and trough outflows (Athanase et al., 2020; Rudels et al., 2015). Kawasaki and Hasumi (2016) studied the AW inflow at the Fram Strait by using an ice-ocean model and provided a quantitative analysis of the heat transport. According to their findings, the heat flux is lost through: (I) transporting westward (47%); (II) sea surface cooling (16%); (III) injection into the Arctic Ocean interior (37%). They reported that the interannual variability of heat transport toward the Arctic Ocean has strong links to the Sea Level Pressure (SLP) variability modulated by the NAO index.

The Barents Sea is a marginal sea of the Arctic Ocean with a rather shallow continental shelf (average depth ~250 m). The BSO is a hydrographic gateway between Bear Island and the northern end of Norway at the western boundary of the Barents Sea. It is another route, although a shallow one, for the AW entering the Arctic Ocean. After passing through the Norwegian Sea, the AW splits from the Norwegian Atlantic Current (NAC) and then enters the Barents Sea through the BSO. The circulation of the AW in the Barents Sea is greatly confined by

the regional bathymetry, especially the shallow area (Oziel et al., 2016). The southern and central parts of the Barents Sea are permanently sea ice free, so the AW is exposed to the air directly and experiences substantial sea surface cooling. When the AW reaches the northern Barents Sea, which is normally ice covered during winter, its heat is further lost through interacting with the sea ice (Rudels et al., 2015; Smedsrud et al., 2010). The winter sea ice cover reduction in the northern and eastern Barents Sea has become particularly pronounced since 1979 (Onarheim & Årthun, 2017), thus the coupling between the atmospheric forcing and ice-free ocean has been enhanced at these regions. The Barents Sea has become a key area for the water mass transformation induced by the surface buoyancy fluxes. The heat transport through the BSO is closely related to the amount of the volume transport and the inflow temperature. It is the most crucial heat supply to the Barents Sea that helps maintain its largely ice-free ocean status. Mechanisms interfering with the interannual variability of the heat transport through the BSO are explained by Wang et al., (2019). They state that half of the variability is caused by the local wind forcing which contributes to the variation in volume transport by changing the Sea Surface Height (SSH) gradient across the BSO. The other half is controlled by the wind and buoyancy forcing from upstream as a result of the changes in both the volume transport and temperature.

As the FSBW and BSBW meet and mix at the St. Anna Trough (SAT), the merged AW boundary current (AWBC) continues to flow along the continental margin of the Eurasian Basin cyclonically. When the boundary current reaches the Lomonosov ridge, where the section we call S3 is located (Figure 1), it bifurcates into two branches. We define section S4 to document the flow progressing along the ridge, while our section S6 keeps track of the portion continuing into the Canadian Basin (Figure 1). The AWBC is strongly topographically steered, following around bathymetric contours in the Arctic Basin. Timmermans & Marshall, (2020) discussed the controlling mechanisms of the circulation from two perspectives: one is from buoyancy-driven processes based on a double-layer estuary framework, with the ArW in the upper layer and AW below. The AW inflow is driven by the freshwater input, PW inflow flux, and the AW entrainment and mixing between two layers; the other perspective is from wind-driven flow along potential vorticity contours that is regulated by seafloor topography. It is set by the anticyclonic wind-stress in the Beaufort Gyre region and the cyclonic atmospheric forcing in the Nordic Seas. Mooring observations indicate that the AWBC speed decreases gradually from ~20 cm/s near Fram Strait to ~4 cm/s at the Lomonosov Ridge, with the baroclinic nature of the flow in the vertical structure becoming dominated en route (Pnyushkov et al., 2015). The encroachment of the warm and saline AW into the Arctic Ocean refers to "Atlantification" and potentially changes the atmospheric and oceanic circulations, vertical structure, and sea ice condition in the Arctic Ocean. The geostrophic AW volume transport decreases by about one order of magnitude during its progression along the continental slope of the Arctic Basin between the inflow Arctic gateways and the Makarov Basin (Zhurbas & Kuzmina, 2020).

This is accompanied by the weakening of the seasonal signal amplitude in the current speed variability and AW temperature (Pnyushkov et al., 2015). The AW layer will be extensively modified in the warm climate scenario when the local sea ice cover has decreased or the properties of the transported FSBW and BSBW have changed. Polyakov et al., (2017) proposed that sea ice has retreated significantly to the eastern Eurasian Basin owing to the increased AW at mid-depth, which favors surface heat loss to the atmosphere and renders strong local winter ventilation. The surface heat loss is thus supported by the enhanced upward heat transfer from the AW layer. The circumstance of how the changes in FSBW and BSBW affect the AW layer will be later discussed in this paper.

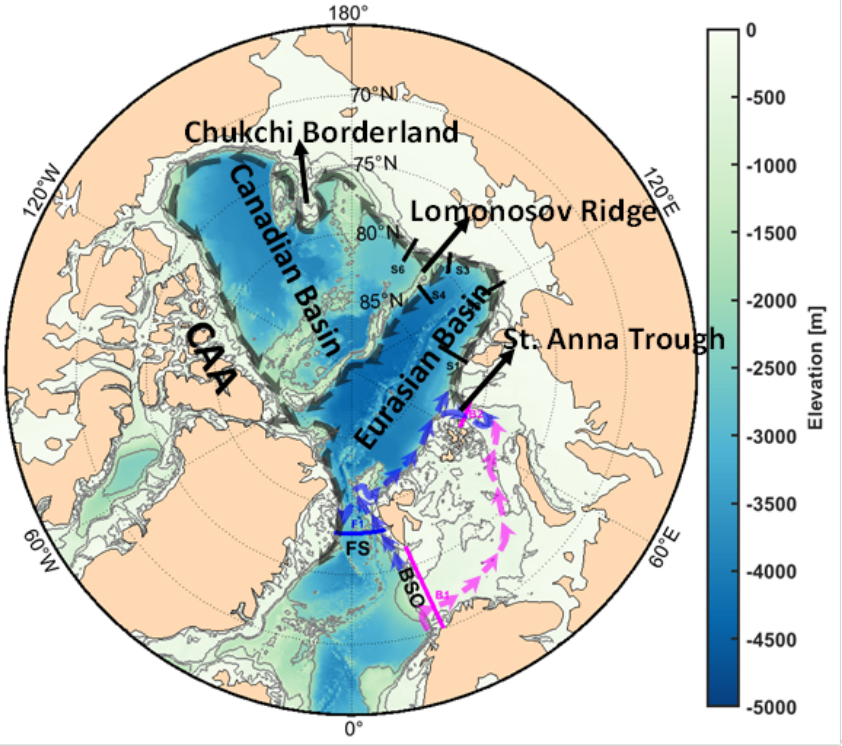

Figure 1. The schematic of the large-scale circulation pattern of the Atlantic Water inflow to the Arctic Ocean, with major geographic features labeled. The blue, magenta, and black lines composed of arrows represent the FSBW, BSBW, and AWBC respectively. The locations of the Arctic gateway straits (F1 and B1) and sections along the poleward pathway (B2, S1, S2, S3, S4 and S6) are indicated. Contour lines are -200 m, -500 m, -1000 m and then -2000 m. FS: Fram Strait, BSO: Barents Sea Opening, CAA: Canadian Arctic Archipelago.

The paper is structured as follows: Section 2 describes the model simulations and introduces the methods and approaches that we use in the analysis. Section 3.1 gives a census of the water masses at Fram Strait and the BSO in the

model with a focus on the thermohaline structure and strength of the FSBW and BSBW. Section 3.2 assesses the temporal variability of the AW volume and heat transport at Fram Strait and the BSO, and also compares the mean state over 2011-2019 from the simulated results and the observations. Section 3.3 covers the AW's poleward pathways from the FSBW and BSBW within the Arctic Ocean. In Section 3.4, we introduce the CAW that is below the standard temperature range and propose its sources. We then further analyze the transformation rate exerted from surface heat and freshwater fluxes to investigate the driving mechanisms of CAW formation in Section 3.5. Lastly, Section 4 concludes the study and discusses its limitations.

2 Numerical Methods

2.1 Numerical Model Description and Setup

In this study, a state-of-art modelling framework called Nucleus for European Modelling of the Ocean (NEMO) version 3.4 is used. It includes a three-dimensional, eddy-permitting and primitive-equation ocean general circulation model Océan PArallélisé (OPA), and the sea ice model Louvain-la-neuve Ice Model version 2 (LIM2) with a modified elastic-viscous-plastic ice rheology, and has thermodynamic and dynamic processes (Fichefet & Maqueda, 1997; Hunke & Dukowicz, 1997; Madec, 2016).

A regional configuration of the interactively coupled ocean-sea ice model covering the Arctic and the Northern Hemispheric Atlantic (ANHA) is applied to carry out the numerical simulations. Two different resolutions of the configuration are used. The model grid mesh has an eddy-permitting resolution of 1/4° (hereafter ANHA4, 544×800 grid points at each vertical level) and a of 1/12° configuration (hereafter ANHA12, 1632×2400 grid) (Hu et al., 2019), extracted from the corresponding global ORCA tripolar grids. In ANHA12, the finest grid spacingis ~1.9 km in Dease Strait, close to the artificial pole over northern Canada, while the coarsest grid spacing is ~9.3 km at the equator. The horizontal resolution at Fram Strait and the BSO is close to 4 km, and around 13 km in ANHA4. There are 50 geopotential vertical levels with the maximum ocean depth at 5727.92 m. Higher vertical resolution is applied to the upper ocean (<2 m resolution for top 10 m) with layer thickness increasing non-linearly from 1.05 m at the surface to 453.14m at the last level. The bathymetry for the Arctic Ocean region stems from the 1 arc-minute global relief model of Earth's surface (ETOPO1) built from NOAA dataset, and the bottom topography (seafloor) is significantly improved by using partial steps (Bernard et al., 2006).

The integration of the ANHA12 simulation starts from January 2002 to the end of December 2019 with 5-day average output. The timespan of 2011-2019 is chosen for our analysis to avoid the model spin-up. The initial conditions, including 3D ocean fields (temperature, salinity, zonal and meridional velocities) as well as 2D sea surface height and sea ice fields (sea ice concentration and thickness), are obtained from the GLobal Ocean ReanalYsis and Simulations 2 version 3 (GLORYS2v3) produced by Mercator Ocean (Masina et al., 2017).

There are two open boundaries for the configuration, one is close to Bering Strait in the Pacific Ocean and the other one aligns at 20°S across the South Atlantic Ocean. Monthly open boundary conditions (temperature, salinity and horizontal ocean velocities) are also derived from GLORYS2v3 dataset. The high temporal (hourly) and spatial (33 km) resolution atmospheric forcing acting on the sea surface, including 10-m surface wind, 2-m air temperature, specific humidity, total precipitation as well as surface downwelling shortwave and longwave radiative fluxes, are taken from the Canadian Meteorological Centre's (CMC) Global Deterministic Prediction System (GDPS) ReForcasts (CGRF) dataset (Smith et al., 2014). The baroclinic model time step is 180s for ANHA12 and 1080s for ANHA4. No temperature and salinity are restored so that the output represents the physical processes of the ocean model. The global monthly river discharge data ($1^\circ \times 1^\circ$) from Dai et al. (2009) and the interannual monthly Greenland meltwater data ($5\ km \times 5\ km$) provided by Bamber et al. (2012) are remapped onto the model grid. The river runoff dataset is from Global River Flow and Continental Discharge Dataset (Dai & Trenberth, 2002). Tides are not taken into consideration in the numerical experiments except for Video 1 in the supplementary material where we use the updated version of ANHA4 (Table 1). The updated ANHA4 is based on NEMO 3.6, a successor of NEMO 3.4. It also uses the HYdrological Predictions for the Environment (HYPE) modeled runoff dataset that covers both major rivers and local runoff (Stadnyk et al., 2021).

Table 1. NEMO Experiments using the ANHA configuration.

Simulation	ANHA12-EXH006	ANHA4-EXH015	ANHA4-ECF002
Ocean Model	NEMO 3.4	NEMO 3.4	NEMO 3.6
Integration	-2019	-2016	-2019m06
Sea Ice Model	LIM2	LIM2	LIM2
Initial Condition	GLORYS2v3	GLORYS2v3	GLORYS2v3
Open Boundary Condition	GLORYS2v3	GLORYS2v3	GLORYS2v3
Atmospheric Forcing	CGRF	CGRF	CGRF
Runoff	Dai and Trenberth runoff and Greenland melt	Dai and Trenberth runoff and Greenland melt	HYPE
Tides	No	No	Yes
Output	-day NORMAL	-day NORMAL	-day NORMAL

2.2 Ariane and Online Passive Tracers

Ariane is a practical offline particle-tracking software package using the Lagrangian method (Blanke, 2002), which is helpful to explore the large-scale ocean circulation of a particular water mass at fairly low computational cost. Unlike the application of the online passive tracers, it avoids running multiple model simulations. We compute the 3D particle trajectories changing with time using Ariane from a modelled ocean velocity field, so that we can track the Atlantic inflow and analyze its paths. Each particle retains its infinitesimal volume over the course of the integration. Although dynamic processes such as diffusion and convective mixing cannot be represented from the Lagrangian tracking, the Eulerian output fields from the ocean model have included these effects and the temperature, salinity and density of each particle evolve based on such fields (Kelly et al., 2018). Therefore, Ariane should produce a reliable representation of the particle pathways. Here, the release of the virtual particles is based on the fields provided by the ANHA12 output. The calculation of how many particles to release in each grid cell is according to this formula.

$$n = N \times \frac{V}{V_{\text{total}}} \times \frac{v}{v_{\text{mean}}}$$

where n is the number of the particles in an identified grid cell along the sections (FS, BSO, and B2) and N is the sum of all the particles at each identified grid cell; V is the volume of each identified grid cell (m^3) and V_{total} is the total volume of identified grid cells (m^3); v is the velocity of each identified grid cell (m/s) and v_{mean} is the mean velocity of all the identified grid cells (m/s). The grid cell is identified when it meets the thermohaline criteria of the AW or the CAW defined for that section and has a positive velocity indicating flowing toward to the Arctic Ocean.

Following the method from (Hu et al., 2019), online passive tracers are applied to trace the AW inflow to the Arctic Ocean from Fram Strait and the BSO, starting from January 1, 2002. Since online passive tracers are embedded in the ocean model, the dynamical processes are well resolved, so that it can represent the pathway of the water mass more accurately. The passive tracer concentration is a non-dimensional quantity as a ratio of the volume of a water mass entering a grid cell over the volume of the grid cell, so an increment ΔC is proportional to the amount of the volume flux:

$$\Delta C = \frac{e1v \cdot e3v \cdot v}{e1t \cdot e2t \cdot e3t}\mathrm{dt}$$

then the vertically integrated tracer concentration could be described as:

$$Cv = \int_z^0 \Delta C(x, y, z, t)\mathrm{dz}$$

where $e1v$ is along-section grid length (m), $e3v$ is the corresponding grid cell thickness (m), v is the velocity perpendicular to the section (m/s), dt is model time step (s), $e1t,\ e2t\ and\ e3t$ are the grid length scales for T grid points (m), z is the largest depth that tracers could reach. Like the Ariane tracers above, these passive tracers are released if they are in the AW temperature and salinity ranges, and their velocity is towards the Arctic Ocean.

2.3 Transport and Content Calculations

The volume and heat transport and freshwater and heat content can be computed from the 5-day mean output from the numerical model as follows:

The volume transport $(Sv,\ 1Sv = 10^6 m^3/s)$:

$$T_{\mathrm{Vol}} = \int_0^S v_i dS = \iint_{-D}^0 v_i \mathrm{dldz}$$

The heat transport $(kW\ or\ kJ/s)$:

$$T_H = \int_0^S v_i \rho_o C_p \left(\theta_i - \theta_{\mathrm{ref}}\right) dS = \iint_{-D}^0 v_i \rho_o C_p \left(\theta_i - \theta_{\mathrm{ref}}\right) \mathrm{dldz}$$

where v_i is the cross-strait seawater velocity at each model grid cell (m/s), dS is the differential area of the section (m^2), dl is the differential length of the section (m), dz is the differential depth (m), θ_i is the seawater potential temperature (℃), θ_{ref} is the reference temperature (0 ℃); ρ_o is the reference density of the seawater $(1,030\ kg/m^3)$, C_p is the specific heat capacity of the seawater $(4.0 \times 10^3\ J/kg \bullet ℃)$.

$$V_{\mathrm{FW}} = \int_0^V \left(\frac{S_{\mathrm{ref}} - S_i}{S_{\mathrm{ref}}}\right) dV = \iint_{-D}^0 \left(\frac{S_{\mathrm{ref}} - S_i}{S_{\mathrm{ref}}}\right) \mathrm{dAdz}$$

The heat content (kJ):

$$H = \int_0^V \rho_o C_p \left(\theta_i - \theta_{\mathrm{ref}}\right) dV = \iint_{-D}^0 \rho_o C_p \left(\theta_i - \theta_{\mathrm{ref}}\right) \mathrm{dAdz}$$

where S_{ref} is the reference salinity (34.8), dV is the differential volume of the domain, dA is the differential area of the horizontal domain (m^2). D is the largest depth of the domain (m).

2.4 Air-Sea Transformation Estimates

Adapting from Myers & Donnelly (2008) and Petit et al., (2020) that are based on an approach originally presented in Speer & Tziperman, (1992), we come up with an approach to quantify the transformation to the CAW based on its

temperature and salinity characteristics (T<0℃, S>34.8). The transformation is in response to the forcings from the surface heat and freshwater fluxes.

where α is the thermal expansion coefficient, β is haline contraction coefficient, C_p is the specific heat capacity, Q is the net surface heat flux into the ocean, that is a combination of the shortwave and longwave radiation, and the sensible and latent heat fluxes ($Q = Q_{\mathrm{SW}} + Q_{\mathrm{LW}} + Q_L + Q_S$), H is the net surface freshwater flux that comes from evaporation minus precipitation (E-P). We do not take sea ice melting and freezing into account because while it may impact the surface water properties, salinity in particular, it will not directly transform the waters. The runoff discharge only produces a transformation to a less dense water mass and mainly takes effect in summer, so it is neglected in our calculation. ρ is the surface density, S is the surface salinity, σ is the surface density anomaly ($\rho - 1000$), σ^* is the middle value of the density bin and $\Delta\sigma$ is the width of the density bin that is set at $\Delta\sigma$= 0.05 kg/m^3 taking into account both resolution and noise (Speer & Tziperman, 1992).

We diagnose evaporation (E) via the specific humidity at the sea surface and compare against the specific humidity of the air. It is computed from the Coordinated Ocean-ice Reference Experiments (CORE) bulk formulae (Large & Yeager, 2009). Precipitation (P) is comprised of snowfall and rain that is directly derived from the atmospheric forcing dataset CGRF. The transformation rate at a particular density bin represents the volume of the water mass that transforms to denser water mass, or less dense water mass, depending on the sign. Surface buoyancy fluxes produce transformation when the surface density is within the density bin, and the temperature and salinity also meet the criteria for the CAW. In our simulation, more dense water being formed would represent an increase in the CAW formation.

3 Results

3.1 Thermohaline Structure of the AW at Fram Strait and the BSO

We first evaluate the hydrographic properties (temperature, salinity and cross-section velocity) of the model water masses at Fram Strait and the BSO in the chosen year of 2013, as shown in Figure 2 (the rationale of choosing this year will be revealed in section 3.4). At Fram Strait, the modelled temperature and velocity fields generally coincide with the observational measurements by the mooring arrays from Beszczynska-Möller et al, (2012). The thermohaline structure of water masses at Fram Strait is characterised by the warm and saline AW inflow at the eastern shelf and cold and fresh Arctic Water outflow at the other side. Both have the temperature and salinity cores along the shelf near the surface with the annual mean velocity cores exceeding 10 cm/s. Compared to the Arctic Water outflow, the AW inflow is less baroclinic so that the velocity core reaches deeper to a depth of near 700 m. The temperature and salinity fields demonstrate a similar contour pattern and the temperature and salinity cores extend further to the west in the strait. The AW recirculation branches, which are considered as return flows of the WSC offshore branches, can be

observed in central Fram Strait from the cross-section velocity plot (Figure 2c). The bulk AW recirculation is driven by the seasonally varying mesoscale eddy activity (Hattermann et al., 2016). The drastic lateral density gradient between these two water masses potentially enhances the baroclinic instability at Fram Strait and thus greatly catalyzes the abundant eddy generation (Wekerle et al., 2020).

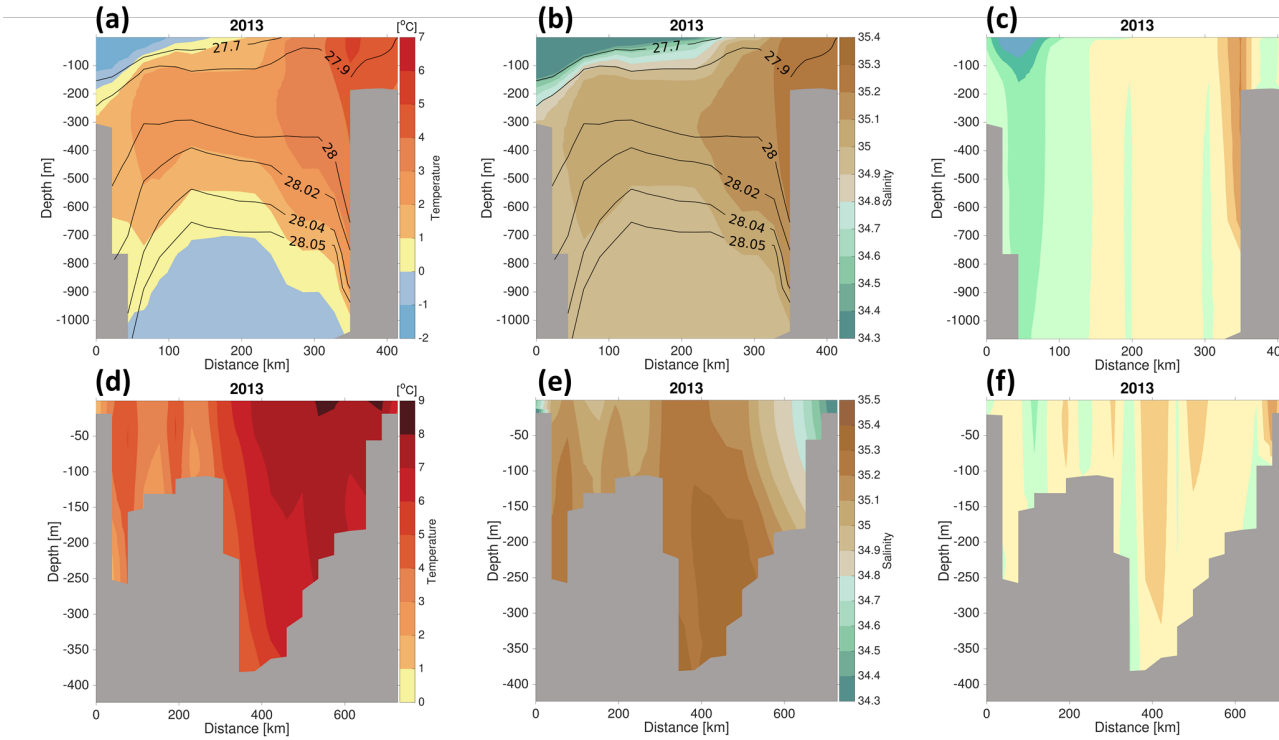

Figure 2. Annual mean temperature T (a & d, unit: ℃), salinity S (b & e), and normal to cross section velocity v (c & f, unit: cm/s) at Fram Strait (Upper panel) and the BSO (Lower panel) in 2013. The velocity is positive towards the Arctic Ocean. The isopycnal lines are contoured onto the temperature and salinity fields in Fram Strait. The x-axis shows the distance (Fram Strait: from west to east; BSO: from north to south) in kilometres and y-axis show the ocean depth in metres.

We define the AW as having temperature greater than 2 ℃ and salinity greater than 34.8, adapted from Beszczynska-Möller et al., (2012) who only used T>2 ℃ without salinity constraint. From their study, the mean observed temperature of the AW inflow at Fram Strait over 1997-2010 was 3.1 $\pm$ 0.1 ℃. The simulated mean temperature of the AW inflow from our model is about 1 ℃ warmer, 3.85 $\pm$ 0.01 ℃ in ANHA12 over 2011-2019 and 4.14 $\pm$ 0.01 ℃ in ANHA4 over

2011-2016 (Table 2). The comparisons show that our model tends to simulate a warmer AW, but it might also be due to the warming trend over recent years. We detail the interannual and seasonal variability of the thermohaline structure of the AW in Fram Strait in Figure S1 and S2. The temperature core for the AW is maximum in 2017, reaching 6 ℃. This is accompanied by a strong northward flow at a velocity of over 15 cm/s. With regard to the seasonal cycle, the temperature core is cooler in the winter and spring months, typically under 5 ℃. It warms in the summer on account of seasonal surface warming. The salinity core does not show any obvious seasonality. Therefore, more buoyant waters can be found above 200 m depth in the summer and fall, indicated by the deeper depth of the isopycnal line $\sigma = 27.9\ kg/m^3$.

Table 2. Long-term means of the AW temperature, oceanic volume and heat transport through Fram Strait and the BSO from ANHA4, ANHA12 and available observations. ANHA4: averaged over 2011-2016; ANHA12: averaged over 2011-2019; a: Mean over 1997-2010 from Beszczynska-Möller et al. (2012); b: Mean over 1997-2006 from Schauer et al. (2008); c: Mean over 1997-2007 from Smedsrud et al. (2010)

Sections	Fram Strait	BSO	
AW Definitions	T > 2, S>34.8	T > 3, S > 34.8	
ANHA4	Volume Transport (Sv)	3.2±0.5	2.7±0.3
	Heat Transport (TW)	60.8±3.2	78.3±9.8
ANHA12	Volume Transport (Sv)	2.4±0.4	2.9±0.3
	Heat Transport (TW)	45.6±7.5	86.3±7.0
Observations	Volume Transport (Sv)	3.0±0.2[a]	3.2[c]
	Heat Transport (TW)	26-50[b]	73[c]

In contrast to Fram Strait, the BSO is a much broader and shallower Arctic gateway. Since there is a higher temperature core of up to 9 ℃ in the model, we define the AW thresholds as the temperature being greater than 3 ℃ and the salinity greater than 34.8 for the BSO, consistent with Oziel et al., (2016). The model successfully captures some fundamental features of the dynamic structure of the water masses, as observed in Ingvaldsen et al., (2004) and Skagseth et al., (2008). Along the Norwegian Coast, the temperature core does not overlap the salinity core, but with the freshest water, which means water containing a great amount of heat could be fresh referenced to a salinity of 34.8. This fraction of the warm and fresh water mass is carried by the Norwegian Coastal Current that is not primarily of Atlantic origin. The AW inflow through the BSO is manifested as a wide branch near the central section reaching the deeper part of the BSO and a relatively narrow branch sitting to the south. The mean AW inflow is a barotropic structure as the cores show uniform vertical velocity profiles. Compared to the annual mean velocity in Fram Strait, the mean AW inflow speed crossing the BSO is weak, of less than 10 cm/s. Other than the AW recirculation branches, there is some relatively colder and fresher water of

Arctic origin above the ridge flowing out of the Barents Sea (Figure 2f).

The mean modelled and observed temperature of the AW inflow in the BSO over the period of 2000-2010 has been estimated as 5.5-6 ℃ and exhibited a warming trend in that decade (Wang et al., 2019). Our simulated temperature average for the AW inflow is calculated to be slightly warmer, 6.00 ± 0.03 ℃ in ANHA12 over 2011-2019 and 6.28 ± 0.03 ℃ in ANHA4 over 2011-2016 (Table 2). We present the interannual and seasonal changes of the thermohaline characteristics of the AW inflow at the BSO in Figure S3 and S4. The banded structure of the velocity field is depicted as two visible AW inflow cores, weaker inflows, return flows and Arctic outflows. They consistently appear each year. The temperature core is more pronounced during 2015-2017. The seasonal variability is substantial with higher temperature cores from August to October and fresher salinity cores from November to March on the southern side along the Norwegian coast, as well as stronger AW inflow cores from November to January.

3.2 Transports through the Fram Strait and BSO

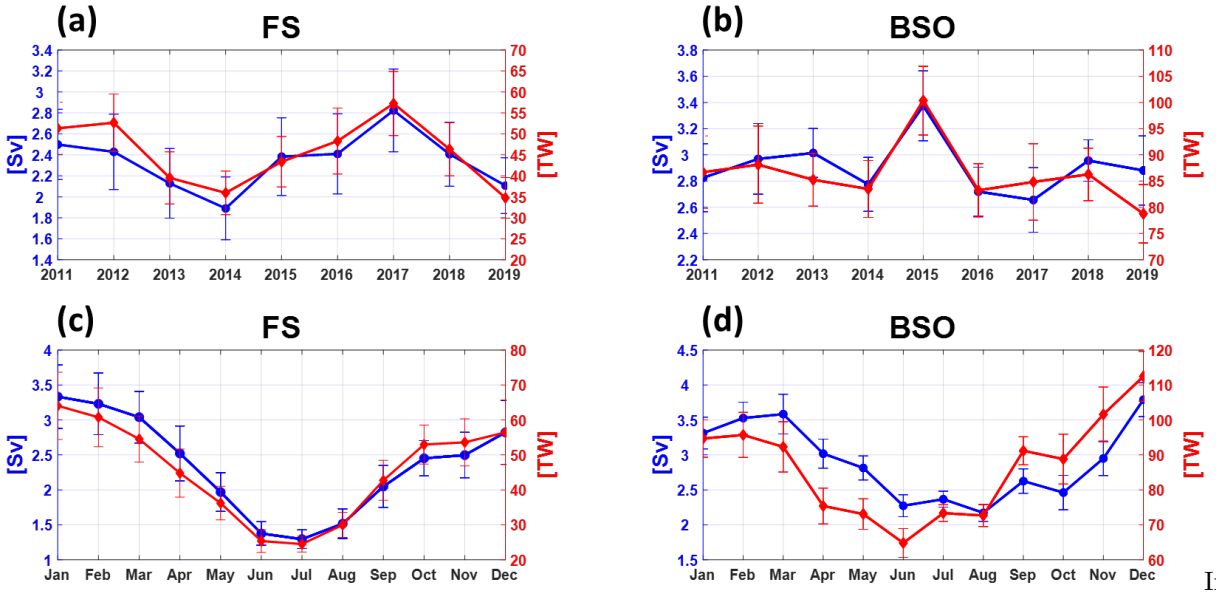

In order to further elucidate the AW inflow variability through these two gateways, we then quantify the AW volume and heat transport on the interannual and seasonal time scales (Figure 3). The volume and heat transport for the AW inflow at Fram Strait are low in 2014 and 2019 (~2 Sv and ~35 TW) and high in 2017 (~2.8 Sv and ~55 TW). The correlation coefficient between the volume and heat transport is 0.93, significant at the 99 % level (p-value=0.0003). The peak-to-peak amplitude of the interannual fluctuation of the volume transport is ~30% of the mean volume transport. The long-term means of volume and heat transport from ANHA4 and ANHA12 are comparable to the mooring results of 3.0 ± 0.2 Sv (Beszczynska-Möller et al., 2012) and 26-50 TW

(Schauer et al., 2008) (Table 2). At the BSO, both volume and heat transport peak in 2015, with the volume transport of ~3.4 Sv and the heat transport of ~100 TW. The correlation coefficient between the volume and heat transport at the BSO is 0.80, significant at the 99 % level (p-value=0.009). From the modelled studies and available observational results, we find that the long-term mean volume transport of the FSBW and BSBW is of the roughly equivalent intensity, ~3 Sv, but the model BSBW plays a relatively larger role in bringing heat into the Arctic Ocean than the FSBW.

Figure 3. Top row: the interannual variability of volume (blue) and heat transport (red) for the Atlantic Water at Fram Strait (a) and the BSO (b) over 2011-2019 with standard error estimates included (stardard deviation over the square root of the number of the data samples). Bottom row: Fram Strait (c) and the BSO (d), but for the seasonal variability. The heat transport is referenced to 0 ℃. Positive values mean towards the Arctic Ocean, i.e. transports are positive northwards across Fram Strait and eastwards across the BSO.

We illustrate the seasonal cycle of the heat and volume transport at Fram Strait (Figure 3c), which is in good agreement with the Figure 4c from Beszczynska-Möller et al., (2012). The volume and heat transport for the AW inflow at Fram Strait reaches its minimum in July (~1.3 Sv and ~25 TW) and maximum in January (~3.3 Sv and ~64 TW), with substantially higher transport in the winter months (January-March). The fluctuation in oceanic heat transport is strongly correlated to the volume transport. The overall annual mean cycle for the AW inflow through the BSO demonstrates a similar variation pattern of low transport in the summer and high transport in the winter, spanning a range from ~2.2 to ~3.8 Sv for volume transport and from ~65 to ~112 TW for heat transport. The summer minima for volume and heat transport at the BSO are not synchronous. The higher AW inflow during fall and winter than summer is largely due to the stronger AW velocity cores in the fall and winter months (Figure S2, S4). This systematic annual cycle is passed down from the upstream transport variability of the eastern branch of the North Atlantic Current in the Norwegian Sea (Ingvaldsen et al., 2004; Orvik et al., 2001), which is induced by the wind pattern variability over the Nordic Seas. The wind forcing pattern is manifested as a strong cyclonic wind stress curl in the winter associated with the Icelandic Low, whose intensity is reflected by a high winter NAO index. Since this distinct seasonal cycle exists in both gateway straits, it is less likely to be on account of their respective local effects.

3.3 AW Inflow Pathway from Online Passive Tracers

Online passive tracers representing the FSBW (T>2 ℃ & S>34.8) and BSBW (T>3 ℃ & S>34.8) are simulated to depict the propagation of the AW inflow in the pan-Arctic region from 2002 to 2018. We attach a video illustrating the changing state during the simulation time (Video S1). We also show a snapshot of the vertically integrated AW tracer concentration on June 4, 2019 (Figure 4). The large-scale circulation of the FSBW features as the circumpolar boundary current, marching along the continental slope and basin edges. It arrives at the

SAT and distributes over the area through the first year and a half. Continuing along its route, it reaches the Lomonosov Ridge and enters the Canadian Basin after roughly three years of the simulation. It first reaches the slope of the Canada Basin in the middle of 2007 and then more tracers accumulates in the Canada Basin. It also gradually accumulates in the interior of the eastern part of the Eurasian Basin and the Makarov Basin. The vertically integrated tracer concentration is approximately 600 m along the margins of the Arctic Basin, whereas the concentration in the central basin in proximity to the CAA is half of that value. In terms of the BSBW, the tracers enter the Arctic Basin through the eastern side of the SAT after passing through the Barents Sea, or flow along the BSO as return flows and then follow the trajectory of the FSBW. The general spatial patterns of the tracers from the two branches are quite similar but still exhibit some discrepancies. The BSBW tracers have the highest concentration in the eastern Arctic Basin in the vicinity of the Lomonosov Ridge. It has two third of the concentration formed by the FSBW tracers toward the end of the simulation (Figure 4). Being constrained by the Chukchi Borderland, the distribution of the BSBW tracers is not significantly high along the slope of the Canada Basin. We notice that the AW tracers are mainly bounded in the Arctic Basin, with only limited loss via Fram Strait and with a smaller portion export via the CAA. Integrating these two branch waters together, the concentration in the eastern Arctic Basin is substantially larger than the other parts of the Arctic Ocean at the end of the integration time (Figure 4a), with a tracer concentration of nearly 1100 m.

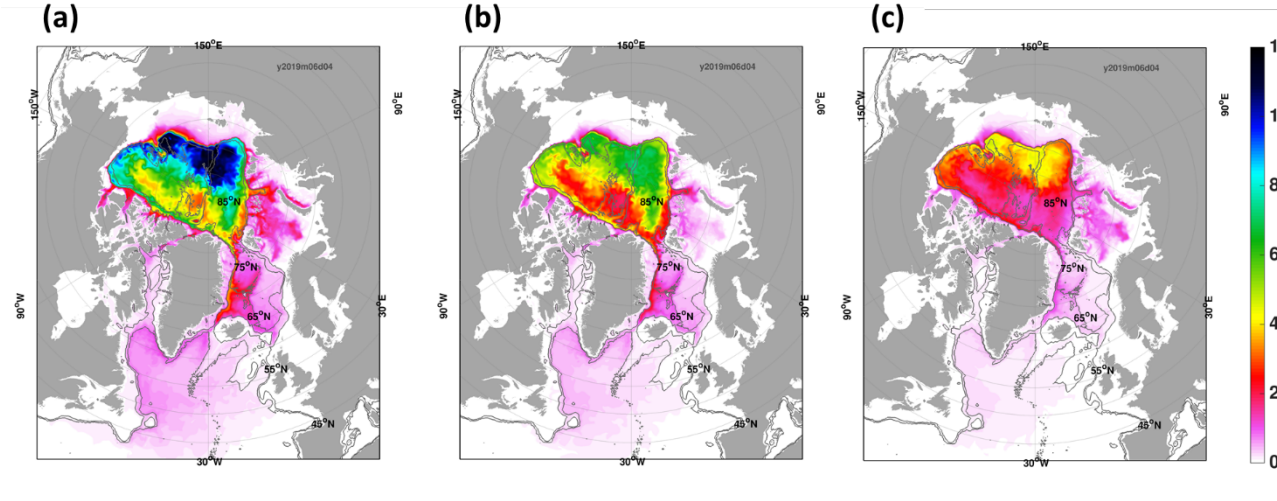

Figure 4. A snapshot of the vertically integrated AW tracer concentration in June 4, 2019 (a) particles are released from a combination of Fram Strait and the BSO; (b) from Fram Strait solely; (c) from the BSO solely.

3.4 The Discovery and Sources of the CAW

We calculate the volume transport for the AW at S3 and S6 based on the definition of T>0 ℃ and S>34.8 (Figure 5), referenced to Dmitrenko et al., (2015) where they defined T>0 ℃ and 34.75<S<34.95 for the FSBW and T>0 ℃ and S>34.9 for the "True" mode of the BSBW in the SAT. Other than the peak shown at the beginning of 2017, the most obvious feature in the timeseries of the transport at S3 is the significant transport reductions in 2013 and 2014, indicated by the shading in Figure 5a. The reductions last for a few months, although the one in 2014 has a longer duration. The volume transport is below 2 Sv during both events. Farther along the pathway at S6, the AW transports reduce to zero, or even reverse in sign during these events. Exploring these events, we originally considered whether the circulation had temporarily reversed. After further study, we found that instead of reversing, the negative transports were associated with the AW being replaced by a colder water mass that did not satisfy the criteria for the AW we had been using. Given that the replacement water mass keeps its salinity properties but with below-zero temperature, we define this water mass as CAW. The CAW also differs from the regular AW with its higher density. We then compute the volume transport of the CAW, which is defined as -1 ℃<T<0 ℃, S>34.8 for B2 and -0.5 ℃<T<0 ℃, S>34.8 for other sections. The pulses of the CAW are clear during 2013 and 2014. The CAW replaces the regular AW and thus causes the reductions in the regular AW transport during the corresponding time periods. The CAW transport increases following its poleward pathway from B2 to S3, and reaches a maximum at S3. The CAW transport at B2 is between 2 and 3 Sv during both events. Increasing by more than twofold from B2, the CAW transport at S3 is 6 Sv in the 2013 event and 7 Sv in 2014. The CAW signal has been greatly amplified at this section. The time lag of one or two months between its upstream sections is expected because of the circulation timescale over a basin-wide area. We do a simple calculation using velocity v=20 cm/s and time t=45 days to get a traveling distance of around 750 km, which is the rough distance between S1 and S2. We do not see the CAW anomaly from the sections we set along the FSBW pathway from Fram Strait to SAT (not shown). We notice that only when the CAW flux at B2 (near SAT) has a large enough volume and duration, can it trigger the domino chain effect of the CAW anomaly signals in the downstream sections. The start and end months of the CAW events at each section are listed in Table 3.

To identify the structure and distribution of the CAW and to uncover its variations within an annual cycle, we illustrate a cross-trough section temperature plot at B2 and the horizontal region temperature plot near SAT in 2014 when a significant CAW anomaly occurs (Figure S5). The hydrographic pattern of the water masses flowing through the SAT is manifested as warm FSBW entering the SAT with a temperature core of 1-2 ℃ along the western flank, the cold and denser BSBW at the opposite side of the trough, and the extremely cold and fresh surface ArW in the top 100 m. These water masses interact and vary throughout the year, but a distinct and unstable vertical density front over the water column consistently exists. From March to August, the CAW sits over the

slope of the eastern side of B2 with a velocity of over 20 cm/s before sinking down to the ocean bottom (Figure S5a and Table 3). It is connected to the surface cold water until it is cut off by the reappearance of the regular AW at the upper slope. From October to December, two AW temperature cores are shown in the transect plot, but they have different origins from the FSBW and BSBW respectively (Figure S5a). Only a small amount of the CAW remains at the ocean bottom close to the eastern side. As the CAW occupies the water column at the depth of 200-500 m, by averaging the temperature field over that depth range from the ocean model, we are able to show where the CAW exists at the entrance from the Barents Sea to the Arctic Basin (Figure S5b). The CAW is clearly visible at the southern and eastern sides of the SAT and the Voronin Trough throughout the CAW anomaly duration. They are combined to drain the CAW from the Barents Sea.

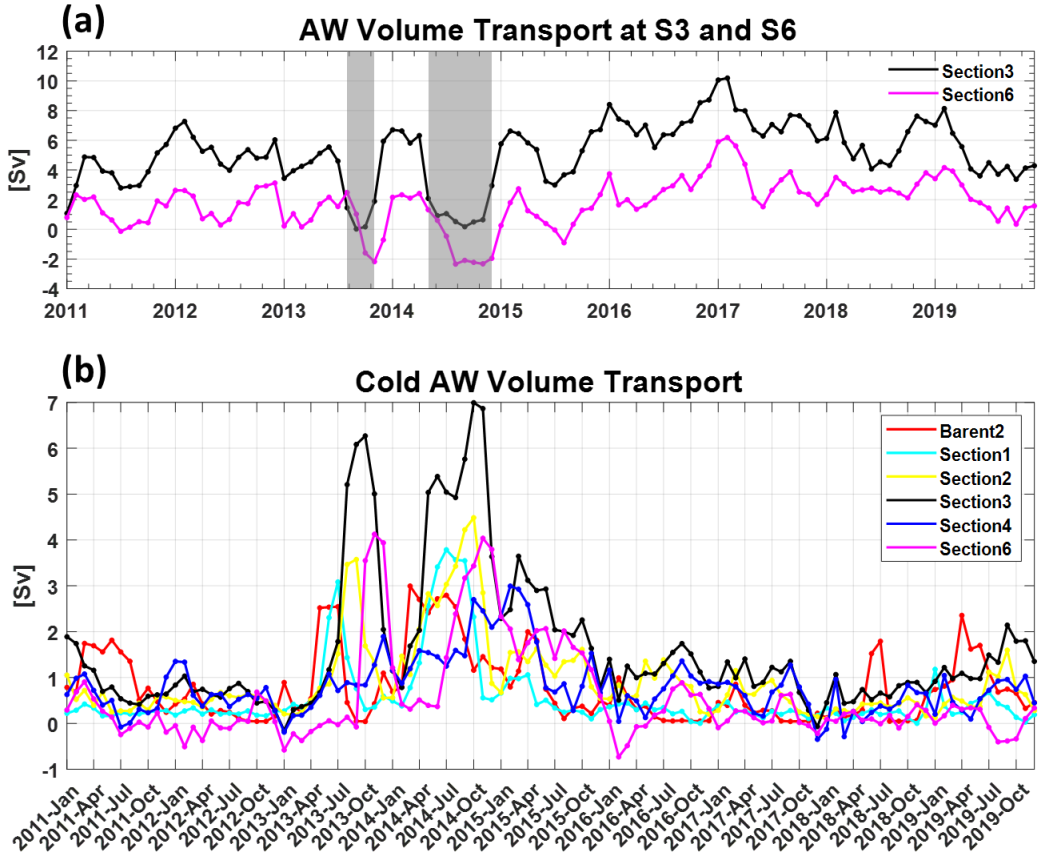

Figure 5. (a) Monthly AW volume transport at S3 from 2011-2019; (b) Monthly CAW volume transport at Barent2 (B2), Section1 (S1), Section2 (S2), Section3 (S3), Section4 (S4) and Section6 (S6) from 2011-2019; The locations of each section are shown in Figure 1.

Table 3. The duration of the apparent CAW signals at some sections in 2013 and 2014. The CAW pulses are apparent when the volume transport is larger than 3 Sv at S3, and it is larger than 2 Sv for the other sections.

Years	2013	2014
B2	May-Jul	Mar-Aug
S1	Jun-Jul	May-Oct
S2	Aug-Sep	Jul-Nov
S3	Aug-Nov	May-Dec
S6	Oct-Dec	Aug-Jan 2015

To probe the source of the CAW, we conduct Ariane experiments for the BSBW and FSBW. Nearly 5000 particles are homogeneously released all at once at the BSO, representing the AW inflow (T>3 ℃, S>34.8 and v>0 m/s). Three experiments start from July of 2012, 2015, and 2017 respectively and run forward in time to the end of 2019. For the first experiment, we plot a snapshot for the temperature of all the particles after two years (Figure 6b). At the end of the first year, the particles cover the whole Barents Sea and begin to enter the Eurasian Basin through SAT. After two years, the distribution of the particles demonstrates a bifurcation near Lomonosov Ridge. The particles get cooled along their poleward pathway, from 5+ ℃ at the BSO to 0- ℃ near Lomonosov Ridge. The first experiment starting from July 2012 has undergone the conditions that triger the CAW production when the particles were passing through the Barents Sea during 2013 and 2014. In this Ariane experiment, the particles with T<0 ℃ at the AW layer (400-1200 m deep) form a clear trajectory along the rim of the eastern Eurasian Basin. Instead, only few dispersed particles along the trajectory are seen in the other two experiments where the particles are seeded from July of 2015 and 2017 (Figure S6b & d). These results using Ariane tracers verify the existence of the CAW events in the ocean model during 2013 and 2014.

We similarly release the particles at Fram Strait, representing the FSBW (T>2 ℃, S>34.8 and v>0 m/s). We notice that a trajectory formed by the cold particles appears again but only in the first experiment where particles are released from July 2012 (Figure S7). Considering that no CAW signal appears in the FSBW before reaching the SAT, we suggest that the FSBW also contributes to the CAW anomaly but in a slightly different way. After flowing along the continental slope, the particles enter the SAT, mix with the BSBW, and get cooled into the CAW. Here we point out that even though we have doubled the number of seeding particles, the trajectory is not as clear as the one shown in Figure 6c, which implies that the primary source of the CAW comes from the BSBW rather than the FSBW.

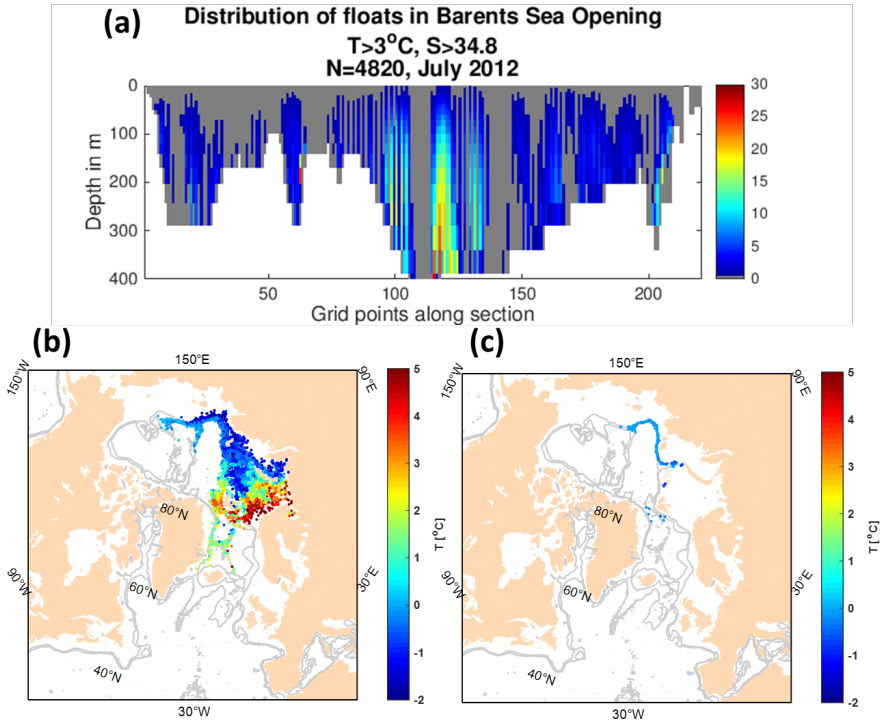

Figure 6. (a) Distribution of particles in the BSO seeded in July 2012. (b) Distribution of all the particles after a two-year forward simulation scheme, that is, a snapshot in July 2014. (c) Only exhibit the particles with a temperature below 0 ℃ at the AW layer (between 400-1200 m deep) from (b).

3.5 Physical mechanisms for the CAW Formation

We now investigate the physical mechanisms causing the CAW production. As the CAW is mainly from the BSBW, the Barents Sea is a breeding ground for the CAW, where the air-ocean coupling heat flux is especially intense (Smedsrud et al., 2013). We simulate the annual mean transformation rate for the CAW in response to surface heat and freshwater fluxes from 2011 to 2019. Taking the year of 2013 for example, when the first CAW event occurs, we first show the transformation rate for the CAW as a function of the surface density (Figure 7a). The positive values represent a removal of buoyancy, which means the water has been densified, hence more CAW is formed. The transformation to the CAW is typically at the isopycnal range of 27.9-28.3 kg/m^3. The heat flux is dominant for the transformation to the denser water mass, whereas the freshwater flux acts to suppress the transformation and has a comparatively little impact. This finding is consistent with Myers & Donnelly, (2008). They found that it is the heat surface flux (primarily sensible heat flux component) that determines the transformation rate of the LSW.

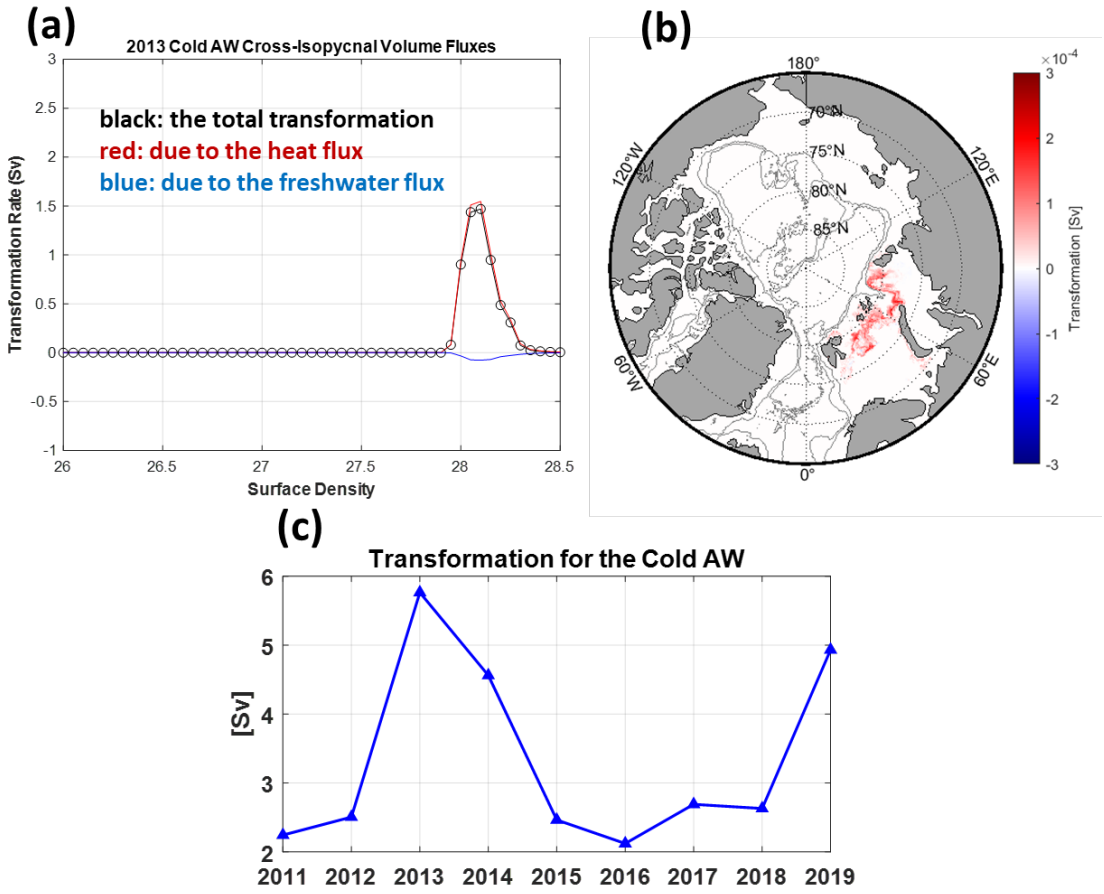

Figure 7. (a) The CAW cross-isopycnal volume fluxes (Sv) changing with the surface density anomaly (kg/m^3) in 2013. The red and blue lines exhibit the transformation rate due to heat and freshwater fluxes, respectively. The black line is the sum of both. (b) the spatial pattern of the transformation rate at σ^*=28.1 $kg/m^3$and $\Delta\sigma$= 0.05 kg/m^3. (c) the interannual variability of the transformation rate for the CAW from 2011 to 2019.

The map in Figure 7b demonstrates the spatial pattern of the transformation at a particular density bin in 2013. It exemplifies that the transformation predominantly occurs in the Barents Sea, especially along the southern and eastern sides of the SAT and in the Voronin Trough where we also can see the CAW (Figure S5). The mean surface heat loss is ~90 W/m^2 and the E-P is ~16 cm/yr for these regions where the transformation into the CAW is most pronounced. Integrating the transformation volume for the CAW in the Barents Sea, we are able to examine the interannual variability of the transformation from 2011 to 2019. The time series Figure 7c presents high transformation rates in two consecutive years, ~5.8 Sv in 2013 and ~4.5 Sv in 2014. The results are consistent with the

pulses of the CAW formation (Figure 5, Table 3). Therefore, the surface heat flux over 2013-2014 at the Barents Sea provides critical preconditioning for the transformation of the AW into the CAW.

3.6 The Evolution and Fate of the CAW

Having explored the origin of the CAW and the processes for its formation, we then investigate the downstream fate of the CAW in the Arctic Basin. We set up another Ariane experiment by releasing around 2000 particles all at once at B2, starting from July 2013. These particles represent the CAW (-1 ℃ $< T <$ 0 ℃, S>34.8) entering the Arctic Basin through the SAT. As we have seen in Figure S5a, the particles sit at the slope of the eastern SAT (Figure 8a). We present the early stages of the evolution after 15 days, 30 days and 50 days of their release (Figure 8b). Only the particles located deeper than 400 m are shown here to avoid too much clutter. Fifteen days after the particles are seeded, the particles still gather together in close proximity at the tongue of the Voronin Trough, lying at the depth range of 400-600 m. After another 15 days has passed, being colder and saltier than the ambient water, the particles start to move deeper downslope while transiting along their poleward pathway. Fifty days from the their release, the particles clearly demonstrate the cascading process that the CAW undergoes, with some distributed near the basin edge of 500 m and successively extending along the 2000 m isobath. At the end of the simulation the particles entering into the Canadian Basin generally reside within the deep layers (>1200 m), whereas the particles staying in the Eurasian Basin spread over the entire depth profile (Figure 8c). Furthermore, the particles in the upper layer (<600 m) tend to reside in the eastern Eurasian Basin while the deep ones settle in the interior of the basin near the side of Lomonosov Ridge.

To further evaluate the impact the CAW anomaly has on the Arctic Basin, we calculate the heat and freshwater content integrated over the whole water column from 2011 to 2019 (Figure 9). We focus on the eastern region covering the CAW trajectory. We also note that the vertically integrated tracer thickness is exceedingly high within the region from our online passive tracer study (Videos S1). The heat content has experienced a significant downturn right after the CAW events in 2013 and 2014. It reaches the minimum in 2015 and then returns back to the previous level. The heat content has reduced by over 50% by 2015 compared to 2013. The decline is dictated by the CAW anomaly signals propagating to the region. The heat content quantifies the heat contained in the AW layer referenced to 0 ℃. The CAW events have negligible impact to the interannual variability of the freshwater content (Figure 9b). The signals have been masked by the strong seasonality that is associated with the sea ice melt and freeze. In contrast to the freshwater content time series, the heat content time series indicates that seasonality has much weaker influence.

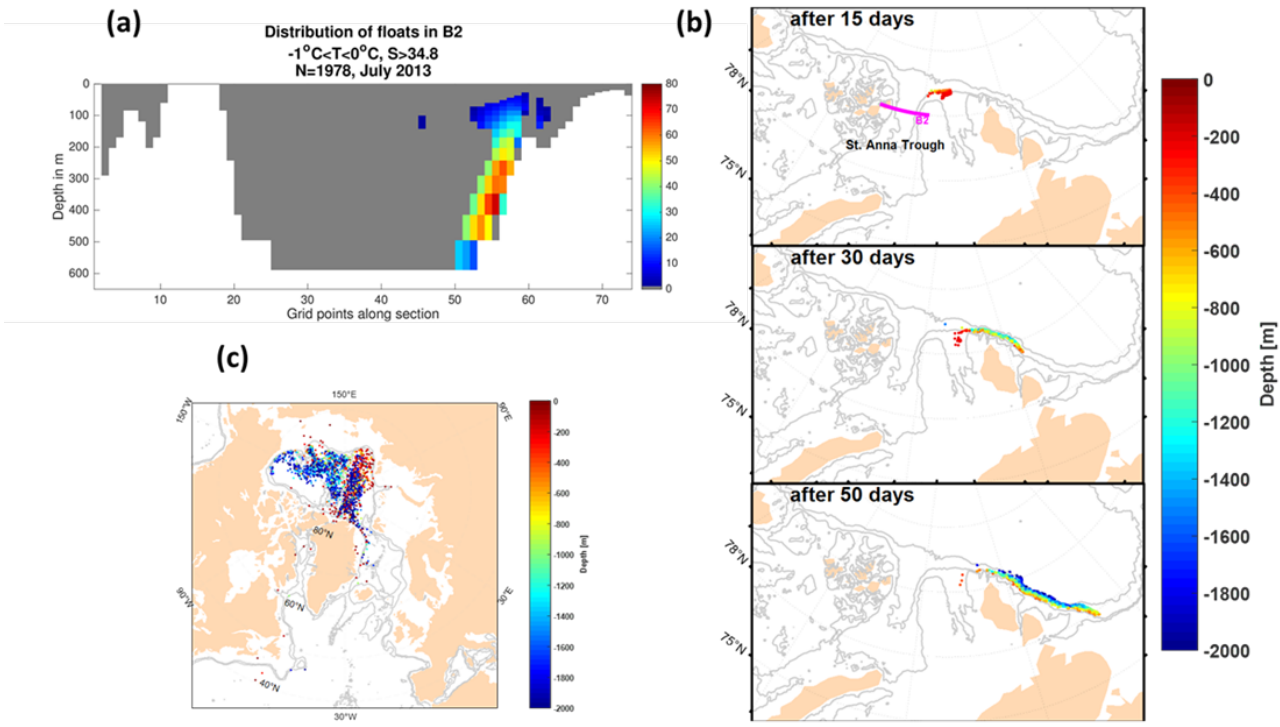

8. (a) Distribution of particles in B2 seeded in July 2013. (b) The locations of the particles after evolving for 15 days, 30 days, and 50 days. (c) The locations of the particles at the end of the simulation, on December 31, 2019.

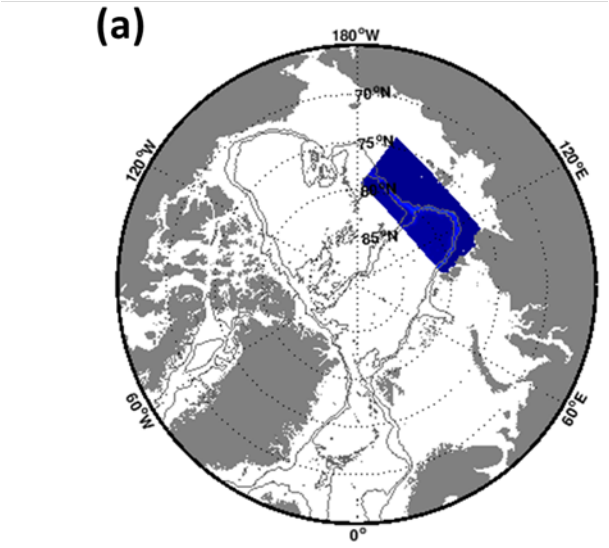

Figure 9. (a) The simulated region in the Arctic Basin, indicated in blue quasi-parallelogram. (b) the heat content and (c) the freshwater content integrated from the whole water column from 2011 to

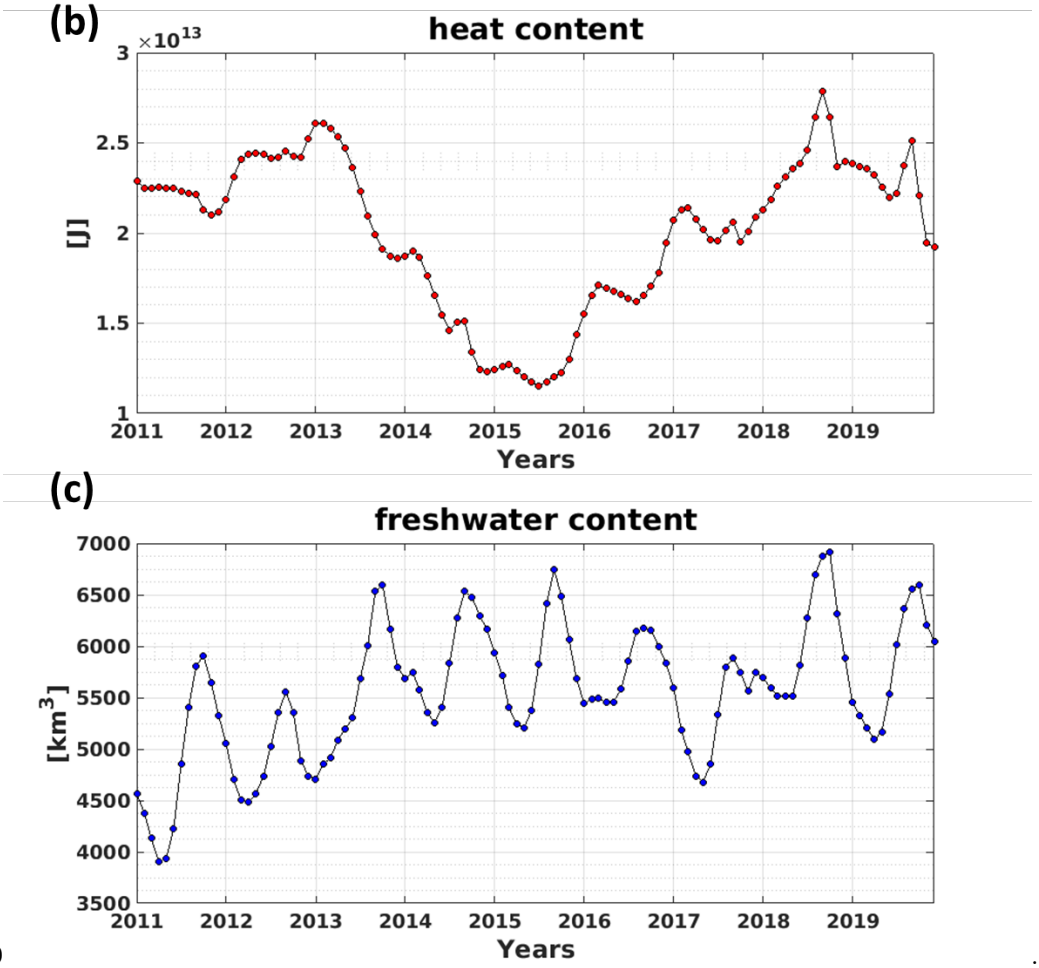

2019 .

4 Summary and Discussion

In this paper, we model the AW in the Arctic Ocean based on its distinct thermohaline properties at two key Arctic gateways – Fram Strait and the BSO. The AW both at Fram Strait and the BSO present clear inflow cores with a more barotropic constituent than the downstream sections (Pnyushkov et al., 2015). The interannual variability of the AW inflow transport at Fram Strait and the BSO exhibits different patterns but the seasonal cycles are more similar. During fall and winter months, the intensified AW inflow flowing at a faster speed facilitates the volume and heat transport through these two sections. The model results from ANHA4 and ANHA12 demonstrate general agreement with the observations regarding long-term means of the volume and heat transport at Fram Strait and the BSO, indicating that we can use the ocean model simulations to study questions of AW propagation in the Arctic Ocean. In comparison to the FSBW, we find that the BSBW is more conducive to transporting heat to the

Arctic Ocean across the entrances. The pathways of the FSBW and BSBW in the Arctic Ocean are depicted using online passive tracers. The tracers concentrate in the eastern Arctic Basin in the proximity of the Lomonosov Ridge. The amount of flux entering the Canada Basin is limited as the tracers are blocked by the Chukchi Borderland (Video 1).

By looking at the transport reductions of the AW at S3 and the transport anomalies of the AW at S6 in 2013 and 2014, we detect the CAW pulses along the rim of the eastern Eurasian Basin. Our results show that the cold dense AW is cascading off the shelf from the eastern flank of the SAT and the Voronin Trough. Studies from Luneva et al., (2020) also shows that St. Anna Trough is one of the most favorable sites that produce the intense dense water descending fluxes. The CAW signals have been markedly amplified when reaching S3 (Figure 5). We speculate that this is due to the considerable mixing/entrainment with the ambient AW along the path to S3, which leads to more surrounding AW transforming to the CAW. The region above the continential slope along the pathway is a mixing hotspot (Schulz et al., 2021). The diapycnal mixing owing to the temperature gradient between the two water masses results in the largest portion of the heat loss of the AW. Our Ariane tracer forward analysis suggests that the source of the CAW is primarily from the BSBW, and with minor contributions from the FSBW. The FSBW contributes to the CAW production by mixing with the BSBW at the eastern SAT. The transformation into the CAW principally occurs at the Barents Sea, and we find that the vigorous and enduring sea surface cooling over 2013-2014 in the Barents Sea provides critical preconditioning for the transformation from the AW to the CAW. Additionally, the warm and saline AW inflows through Fram Strait and the BSO are not high during these two years, which limits heat input to the Barents Sea.

The CAW is not uncommon near the SAT, which we also see from the observational arrays in earlier years, e.g. September 2009 (Dmitrenko et al., 2015; Zhurbas & Kuzmina, 2020). As our analysis suggested, our models are inclined to simulate warmer water than the observations (Table 1), but this cannot alter the perspective that an increasing amount of the colder and denser AW could be produced during 2013-2014. Due to the restricted short simulation period from our study, we could not diagnose the trend of more warm and saline AW flowing into the Arctic Ocean through Fram Strait and the BSO, which acts as a crucial attribute to the Arctic Atlantification (Polyakov et al., 2017). However, the high variability in the AW inflows we have presented in this research can partly account for the AW fluctuations at the AW layer of the Arctic Basin with abrupt cooling/warming events.

The heat transport through the BSO is the prime heat source to the Barents Sea and shows an anticorrelation with the winter Barents Sea ice extent (Årthun et al., 2012; Docquier et al., 2020). As sea ice functions like an insulating layer, the winter sea ice retreat as a result of the Arctic Atlantification makes the Barents Sea more susceptible to the atmospheric forcings, which thus enhances the air-sea heat fluxes (Moore et al., 2022). This scheme thereby increases the

possibility to create appropriate conditions for the CAW formation, which is dependent on the effective region for cooling and less heat transport advected to the area. Farther downstream along the AW progression pathway, the sea ice extent decline also promotes stonger upper-ocean currents and associated vertical shear, coinciding with the enhanced ventilation of the AW and the weakening of stratification in the Eastern Arctic Ocean (Polyakov et al., 2020). All in all, the AW into the Arctic Basin could be cold (T<0 ℃). The CAW has significantly reduced the heat content of the eastern Arctic Basin in 2015 according to our study, and it also has potential impact on the structure of the nutricline and the biological production along the circulation pathways (Jung et al., 2021; Polyakov et al., 2020). However, more future studies are needed to garner a better understanding of its ramifications to the Arctic Ocean under the context of global warming.

Acknowledgments

We gratefully acknowledge the financial and logistic support of grants from the Natural Sciences and Engineering Research Council (NSERC) of Canada. These includes a Discovery Grant (rgpin227438-09) awarded to P.G. Myers, and a Climate Change and Atmospheric Research Grant (VITALS - RGPCC 433898). We are grateful to the NEMO development team and the Drakkar project for providing the model and continuous guidance. We would also like to thank G. Smith for the model atmospheric forcing fields, made available by Environment and Climate Change Canada (http://weather.gc.ca/grib/grib2 glb 25km e.html). We thank Westgrid and Compute Canada for computational resources, where all model experiments were performed. The model code based on the NEMO model is available at https://www.nemo-ocean.eu/ (last access: 28 May 2017, Madec, 2008). Details on the ANHA configuration used are available

at http://knossos.eas.ualberta.ca/anha/index.php (last access: 8 September 2017), with files for the experiment used in this paper at https://doi.org/10.7939/DVN/GIXGXB (Hu, 2020).

References

Athanase, M., Provost, C., Artana, C., Pérez-Hernández, M. D., Sennéchael, N., Bertosio, C., Garric, G., Lellouche, J., & Prandi, P. (2020). Changes in Atlantic Water circulation patterns and volume transports North of Svalbard over the last 12 years (2008-2020). *Journal of Geophysical Research: Oceans*. https://doi.org/10.1029/2020jc016825Bamber, J., Van den Broeke, M., Ettema, J., Lenaerts, J., & Rignot, E. (2012). Recent large increases in freshwater fluxes from Greenland into the North Atlantic. *Geophysical Research Letters*, *39*, L19501. https://doi.org/10.1029/2012gl052552Bernard, B., Madec, G., Penduff, T., Molines, J.-M., Treguier, A.-M., Le Sommer, J., Beckmann, A., Biastoch, A., Böning, C., Dengg, J., Derval, C., Durand, E., Gulev, S., Remy, E., Talandier, C., Theetten, S., Maltrud, M., Mcclean, J., & De Cuevas, B. (2006). *Impact of partial steps and momentum advection schemes in a global ocean circulation model at eddy-permitting resolution.*

56(5–6), 543–567. https://doi.org/10.1007/s10236-006-0082-1Beszczynska-mo, A. (2012). *Variability in Atlantic water temperature and transport at the entrance to the Arctic Ocean, 1997–2010*. *69*, 852–863.Carmack, E. C. (2007). The alpha/beta ocean distinction: A perspective on freshwater fluxes, convection, nutrients and productivity in high-latitude seas. *Deep Sea Research Part II: Topical Studies in Oceanography*, *54*(23–26), 2578–2598. https://doi.org/10.1016/j.dsr2.2007.08.018Cavalieri, D. J., & Parkinson, C. L. (2012). Arctic sea ice variability and trends, 1979-2010. *Cryosphere*, *6*(4), 881–889. https://doi.org/10.5194/tc-6-881-2012Comiso, J. C. (2012). Large decadal decline of the arctic multiyear ice cover. *Journal of Climate*, *25*(4), 1176–1193. https://doi.org/10.1175/JCLI-D-11-00113.1Comiso, J. C., Meier, W. N., & Gersten, R. (2017). Variability and trends in the Arctic Sea ice cover: Results from different techniques. *Journal of Geophysical Research: Oceans*, *122*(8), 6883–6900. https://doi.org/10.1002/2017JC012768Crews, L., Sundfjord, A., & Hattermann, T. (2019). How the Yermak Pass Branch Regulates Atlantic Water Inflow to the Arctic Ocean. *Journal of Geophysical Research: Oceans*, *124*(1), 267–280. https://doi.org/10.1029/2018jc014476Dai, A., Qian, T., Trenberth, K. E., & Milliman, J. D. (2009). Changes in Continental Freshwater Discharge from 1948 to 2004. *Journal of Climate*, *22*(10), 2773–2792. https://doi.org/10.1175/2008jcli2592.1Dai, A., & Trenberth, K. E. (2002). Estimates of Freshwater Discharge from Continents: Latitudinal and Seasonal Variations. *Journal of Hydrometeorology*, *3*(6), 660–687. https://doi.org/10.1175/1525-7541(2002)003<0660:eofdfc>2.0.co;2Dmitrenko, I. A., Rudels, B., Kirillov, S. A., Aksenov, Y. O., Lien, V. S., Ivanov, V. V, Schauer, U., Polyakov, I. V, Coward, A., & Barber, D. G. (2015). Atlantic water flow into the Arctic Ocean through the St. Anna Trough in the northern Kara Sea. *Journal of Geophysical Research: Oceans*, *120*(7), 5158–5178. https://doi.org/10.1002/2015jc010804Fichefet, T., & Maqueda, M. A. M. (1997). *Sensitivity of a global sea ice model to the treatment of ice thermodynamics and dynamics*. *102*(C6), 12609–12646. https://doi.org/10.1029/97jc00480Grivault, N., Hu, X., & Myers, P. G. (2018). Impact of the Surface Stress on the Volume and Freshwater Transport Through the Canadian Arctic Archipelago From a High-Resolution Numerical Simulation. *Journal of Geophysical Research: Oceans*, *123*(12), 9038–9060. https://doi.org/10.1029/2018JC013984Guarino, M.-V., Sime, L. C., Schröeder, D., Malmierca-Vallet, I., Rosenblum, E., Ringer, M., Ridley, J., Feltham, D., Bitz, C., Steig, E. J., Wolff, E., Stroeve, J., & Sellar, A. (2020). Sea-ice-free Arctic during the Last Interglacial supports fast future loss. *Nature Climate Change*, *10*(10), 928–932. https://doi.org/10.1038/s41558-020-0865-2Hu, X., Myers, P. G., & Lu, Y. (2019). Pacific Water Pathway in the Arctic Ocean and Beaufort Gyre in Two Simulations With Different Horizontal Resolutions. *Journal of Geophysical Research: Oceans*. https://doi.org/10.1029/2019jc015111Hunke, E. C., & Dukowicz, J. K. (1997). *An Elastic–Viscous–Plastic Model for Sea Ice Dynamics*. *27*(9), 1849–1867. https://doi.org/10.1175/1520-0485(1997)027<1849:aevpmf>2.0.co;2Jung, J., Cho, K., Park, T., Yoshizawa, E., Lee, Y., Yang, E. J., Gal, J., Ha, S., Kim,

S., Kang, S., & Grebmeier, J. M. (2021). Atlantic-Origin Cold Saline Water Intrusion and Shoaling of the Nutricline in the Pacific Arctic. *Geophysical Research Letters*, *48*(6). https://doi.org/10.1029/2020gl090907Kawasaki, T., & Hasumi, H. (2016). The inflow of A tlantic water at the F ram S trait and its interannual variability. *Journal of Geophysical Research: Oceans*, *121*(1), 502–519. https://doi.org/10.1002/2015jc011375Large, W. G., & Yeager, S. G. (2009). The global climatology of an interannually varying air - Sea flux data set. *Climate Dynamics*, *33*(2–3), 341–364. https://doi.org/10.1007/s00382-008-0441-3Li, J., Pickart, R. S., Lin, P., Bahr, F., Arrigo, K. R., Juranek, L., & Yang, X. (2020). The Atlantic Water Boundary Current in the Chukchi Borderland and Southern Canada Basin. *Journal of Geophysical Research: Oceans*, *125*(8). https://doi.org/10.1029/2020jc016197Luneva, M. V, Ivanov, V. V, Tuzov, F., Aksenov, Y., Harle, J. D., Kelly, S., & Holt, J. T. (2020). Hotspots of Dense Water Cascading in the Arctic Ocean: Implications for the Pacific Water Pathways. *Journal of Geophysical Research: Oceans*, *125*(10). https://doi.org/10.1029/2020jc016044Madec, G. (2016). *NEMO ocean engine*. *27*.Masina, S., Storto, A., Ferry, N., Valdivieso, M., Haines, K., Balmaseda, M., Zuo, H., Drevillon, M., & Parent, L. (2017). An ensemble of eddy-permitting global ocean reanalyses from the MyOcean project. *Climate Dynamics*, *49*(3), 813–841. https://doi.org/10.1007/s00382-015-2728-5Menze, S., Ingvaldsen, R. B., Haugan, P., Fer, I., Sundfjord, A., Beszczynska-Moeller, A., & Falk-Petersen, S. (2019). Atlantic Water Pathways Along the North-Western Svalbard Shelf Mapped Using Vessel-Mounted Current Profilers. *Journal of Geophysical Research: Oceans*, *124*(3), 1699–1716. https://doi.org/10.1029/2018jc014299Muilwijk, M., Smedsrud, L. H., Ilicak, M., & Drange, H. (2018). Atlantic Water Heat Transport Variability in the 20th Century Arctic Ocean From a Global Ocean Model and Observations. *Journal of Geophysical Research: Oceans*, *123*(11), 8159–8179. https://doi.org/10.1029/2018JC014327Onarheim, I. H., & Årthun, M. (2017). Toward an ice-free Barents Sea. *Geophysical Research Letters*, *44*(16), 8387–8395. https://doi.org/10.1002/2017GL074304Oziel, L., Sirven, J., & Gascard, J. C. (2016). The Barents Sea frontal zones and water masses variability (1980-2011). *Ocean Science*, *12*(1), 169–184. https://doi.org/10.5194/os-12-169-2016Pérez-Hernández, M. D., Pickart, R. S., Torres, D. J., Bahr, F., Sundfjord, A., Ingvaldsen, R., Renner, A. H. H., Beszczynska-Möller, A., von Appen, W. J., & Pavlov, V. (2019). Structure, Transport, and Seasonality of the Atlantic Water Boundary Current North of Svalbard: Results From a Yearlong Mooring Array. *Journal of Geophysical Research: Oceans*, *124*(3), 1679–1698. https://doi.org/10.1029/2018JC014759Pnyushkov, A. V., Polyakov, I. V., Ivanov, V. V., Aksenov, Y., Coward, A. C., Janout, M., & Rabe, B. (2015). Structure and variability of the boundary current in the Eurasian Basin of the Arctic Ocean. *Deep-Sea Research Part I: Oceanographic Research Papers*, *101*(March), 80–97. https://doi.org/10.1016/j.dsr.2015.03.001Polyakov, I. V., Alkire, M. B., Bluhm, B. A., Brown, K. A., Carmack, E. C., Chierici, M., Danielson, S. L., Ellingsen, I., Ershova, E. A., Gårdfeldt, K., Ingvaldsen, R. B., Pnyushkov, A. V., Slagstad, D., & Wassmann,

P. (2020). Borealization of the Arctic Ocean in Response to Anomalous Advection From Sub-Arctic Seas. *Frontiers in Marine Science*, *7*(July). https://doi.org/10.3389/fmars.2020.00491Polyakov, I. V., Pnyushkov, A. V., Alkire, M. B., Ashik, I. M., Baumann, T. M., Carmack, E. C., Goszczko, I., Guthrie, J., Ivanov, V. V., Kanzow, T., Krishfield, R., Kwok, R., Sundfjord, A., Morison, J., Rember, R., & Yulin, A. (2017). Greater role for Atlantic inflows on sea-ice loss in the Eurasian Basin of the Arctic Ocean. *Science*, *356*(6335), 285–291. https://doi.org/10.1126/science.aai8204Polyakov, I. V, Rippeth, T. P., Fer, I., Baumann, T. M., Carmack, E. C., Ivanov, V. V, Janout, M., Padman, L., Pnyushkov, A. V, & Rember, R. (2020). Intensification of Near-Surface Currents and Shear in the Eastern Arctic Ocean. *Geophysical Research Letters*, *47*(16). https://doi.org/10.1029/2020gl089469Rudels, B., Korhonen, M., Schauer, U., Pisarev, S., Rabe, B., & Wisotzki, A. (2015). Circulation and transformation of Atlantic water in the Eurasian Basin and the contribution of the Fram Strait inflow branch to the Arctic Ocean heat budget. *Progress in Oceanography*, *132*, 128–152. https://doi.org/10.1016/j.pocean.2014.04.003Schulz, K., Janout, M., Lenn, Y., Ruiz-Castillo, E., Polyakov, I., Mohrholz, V., Tippenhauer, S., Reeve, K. A., Hölemann, J., Rabe, B., & Vredenborg, M. (2021). On the Along-Slope Heat Loss of the Boundary Current in the Eastern Arctic Ocean. *Journal of Geophysical Research: Oceans*, *126*(2). https://doi.org/10.1029/2020jc016375Smedsrud, L. H., Ingvaldsen, R., Nilsen, J. E. Ø., & Skagseth, Ø. (2010). *Heat in the Barents Sea: transport, storage, and surface fluxes*. *6*(1), 219–234. https://doi.org/10.5194/os-6-219-2010Smith, G. C., Roy, F., Mann, P., Dupont, F., Brasnett, B., Lemieux, J.-F., Laroche, S., & Bélair, S. (2014). A new atmospheric dataset for forcing ice-ocean models: Evaluation of reforecasts using the Canadian global deterministic prediction system. *Quarterly Journal of the Royal Meteorological Society*, *140*(680), 881–894. https://doi.org/10.1002/qj.2194Speer, K., & Tziperman, E. (1992). Rates of Water Mass Formation in the North Atlantic Ocean. In *Journal of Physical Oceanography* (Vol. 22, Issue 1, pp. 93–104). https://doi.org/10.1175/1520-0485(1992)022<0093:rowmfi>2.0.co;2Spielhagen, R. F., Werner, K., Sørensen, S. A., Zamelczyk, K., Kandiano, E., Budeus, G., Husum, K., Marchitto, T. M., & Hald, M. (2011). Enhanced modern heat transfer to the arctic by warm atlantic water. *Science*, *331*(6016), 450–453. https://doi.org/10.1126/science.1197397Spreen, G., Steur, L., Divine, D., Geland, S., Hansen, E., & Kwok, R. (2020). Arctic Sea Ice Volume Export Through Fram Strait From 1992 to 2014. *Journal of Geophysical Research: Oceans*, *125*(6). https://doi.org/10.1029/2019jc016039Stadnyk, T. A., Tefs, A., Broesky, M., Déry, S. J., Myers, P. G., Ridenour, N. A., Koenig, K., Vonderbank, L., & Gustafsson, D. (2021). Changing freshwater contributions to the Arctic. *Elementa: Science of the Anthropocene*, *9*(1). https://doi.org/10.1525/elementa.2020.00098Stroeve, J., Holland, M. M., Meier, W., Scambos, T., & Serreze, M. (2007). Arctic sea ice decline: Faster than forecast. *Geophysical Research Letters*, *34*(9), n/a-n/a. https://doi.org/10.1029/2007gl029703Timmermans, M., & Marshall, J. (2020). Understanding Arctic Ocean Circulation: A Review of Ocean Dynamics

in a Changing Climate. *Journal of Geophysical Research: Oceans*, *125*(4). https://doi.org/10.1029/2018jc014378Wang, Q., Wang, X., Wekerle, C., Danilov, S., Jung, T., Koldunov, N., Lind, S., Sein, D., Shu, Q., & Sidorenko, D. (2019). Ocean Heat Transport Into the Barents Sea: Distinct Controls on the Upward Trend and Interannual Variability. *Geophysical Research Letters*, *46*(22), 13180–13190. https://doi.org/10.1029/2019GL083837Wang, Q., Wekerle, C., Wang, X., & Danilov, S. (2020). *Intensification of the Atlantic Water Supply to the Arctic Ocean Through Fram Strait Induced by Arctic Sea Ice Decline*. https://doi.org/10.1029/2019GL086682Wekerle, C., Hattermann, T., Wang, Q., Crews, L., Von Appen, W.-J., & Danilov, S. (2020). Properties and dynamics of mesoscale eddies in Fram Strait from a comparison between two high-resolution ocean–sea ice models. *Ocean Science*, *16*(5), 1225–1246. https://doi.org/10.5194/os-16-1225-2020Woodgate, R. (2013). Arctic Ocean Circulation – going around at the top of the world. *Nature Ed. Knowledge*, *February 2012*, 1–15.Zhurbas, N., & Kuzmina, N. (2020). Variability of the thermohaline structure and transport of Atlantic water in the Arctic Ocean based on NABOS (Nansen and Amundsen Basins Observing System) hydrography data. *Ocean Science*, *16*(2), 405–421. https://doi.org/10.5194/os-16-405-2020